Title

Minimizing Crinkling of Soft Specimens Using Holey Gold Films on Molybdenum Grids for Cryogenic Electron Microscopy

Journal

Microscopy and Microanalysis, 27(4)

ISSN

1431-9276

Authors

Jiang, Xi
Xuan, Sunting
Zuckermann, Ronald N
et al.

Publication Date

2021-08-01

DOI

10.1017/s1431927621000520

Peer reviewed

Minimizing Crinkling of Soft Specimens Using Holey-Gold Films on Molybdenum Grids for Cryogenic Electron Microscopy

Xi Jiang[1], Sunting Xuan[2], Ronald N. Zuckermann[2], Robert M. Glaeser[4], Kenneth H. Downing [4#], Nitash P. Balsara[1,3]*

1. Materials Sciences Division, Lawrence Berkeley National Laboratory, Berkeley, CA 94720, USA2. Molecular Foundry, Lawrence Berkeley National Laboratory, Berkeley, CA 94720, USA

3. Department of Chemical and Biomolecular Engineering, University of California, Berkeley, CA 94720, USA

4. Molecular Biophysics and Integrated Bioimaging, Lawrence Berkeley National Laboratory, Berkeley, CA 94720, USA

Deceased

*Corresponding author: xijiang@lbl.gov

Submission to Microscopy and Microanalysis

Abstract:

We introduce a novel composite holey gold support that prevents cryo-crinkling and reduces beam-induced motion of soft specimens, building on the previously introduced all-gold support. The composite holey gold support for high-resolution cryogenic electron microscopy of soft crystalline membranes was fabricated in two steps. In the first step, a holey gold film was transferred on top of a molybdenum grid. In the second step, a continuous thin carbon film was transferred onto the holey gold film. This support (Au/Mo grid) was used to image crystalline synthetic polymer membranes. The low thermal expansion of Mo is not only expected to avoid cryo-crinkling of the membrane when the grids are cooled to cryogenic temperatures, but it may also act to reduce whatever crinkling existed even before cooling. The Au/Mo grid exhibits excellent performance with specimens tilted to 45°. This is demonstrated by quantifying beam-induced motion and differences in local defocus values. In addition, images of specimens on the Au/Mo grids that are tilted at 45° show high-resolution information of the crystalline membranes that, after lattice-unbending, extends beyond 1.5 Å in the direction perpendicular to the tilt axis.

Keywords:

cryo-EM, crystallography, crystalline polypeptoid membranes, cryo-crinkling, specimen flatness

1. Introduction:

The resolution of structures obtained from radiation-sensitive biological macromolecules using cryogenic electron microscopy (cryo-EM) has significantly improved with the introduction of direct electron detectors and novel image processing algorithms (Cheng, 2015; Kuhlbrandt, 2014; Li, et al., 2013; Scheres, 2012). The high detective quantum efficiency (DQE) of these

detectors and their ability to rapidly record images enable dose-fractionation movies and beam-induced motion correction, and this enhances the resolution of low-dose cryo-EM imaging (Li, et al., 2013; Zheng, et al., 2017).

Images obtained by cryo-EM are also affected by the nature of the support on which the specimens reside. The support affects imaging due to the fact that beam-induced motion becomes a greater problem when crinkling of specimens occurs as they are cooled. Several early studies have investigated the effect that the geometry and materials-composition of the specimen support has on beam-induced motion (Booy & Pawley, 1993; Butt, et al., 1991; Fujiyoshi, 1998; Glaeser, 1992; Gyobu, et al., 2004; Han, et al., 1994; Henderson & Glaeser, 1985; Quispe, et al., 2007; Rhinow & Kuhlbrandt, 2008; Spence, et al., 2003; Vonck, 2000). Rhinow el al. showed that a thin film of the metal glass $Ti_{88}Si_{12}$ on a copper grid reduced beam-induced motion by 50% when compared to an amorphous carbon film under the same conditions (Rhinow & Kuhlbrandt, 2008). Glaeser et al. showed that an ultra-thick carbon support film on a copper grid also reduced beam-induced motion (Glaeser, et al., 2011).

Holey carbon films are commonly used in cryo-EM studies, but specimens supported on them suffer from significant beam-induced motion (Brilot, et al., 2012; Russo & Passmore, 2014). In more recent studies, Russo and Passmore demonstrated that an all-gold supporting grid (UltrAuFoil grid) was able to significantly reduce beam-induced motion in dose-fractionation movies, up to 50-fold along the *z* (vertical) direction and twofold in the *x*-*y* direction, as compared to a holey carbon film on a copper grid (Russo & Passmore, 2014; Russo & Passmore, 2016). The improved image quality was initially attributed to the high electrical conductivity of the holey gold supporting film, but it now seems likely that elimination of cryo-crinkling is an important factor. Reduced cryo-crinkling in the gold/gold supports is also shown in [20]. In any

event, it is now standard to use holey gold films for cryo-EM of suspensions of individual macromolecules in vitrified ice, due to the improved data resolution in single-particle analysis and in tomography (Tan, et al., 2017).

In addition to beam-induced motion, the flatness of the specimen is an important factor that limits resolution of crystalline membranes composed of ordered arrays of either biological or synthetic macromolecules (Booy & Pawley, 1993; Glaeser, 1992; Han, et al., 1994; Nogales, et al., 1995; Vonck, 1996). Unlike well-distributed suspensions of individual macromolecules in vitrified ice, which can be imaged without using a thin supporting film, continuous carbon films are universally used to support crystalline membranes. Carbon supporting films can, however, influence the flatness of the crystalline membranes (Baldwin, et al., 1988; Booy & Pawley, 1993; Butt, et al., 1991; Fujiyoshi, 1998; Glaeser, 1992; Glaeser, et al., 2011; Gyobu, et al., 2004; Han, et al., 1994; Henderson, et al., 1990; Henderson & Glaeser, 1985; Kuhlbrandt, et al., 1994; Nogales, et al., 1995; Vonck, 1996; Vonck, 2000; Walz, et al., 1997). The crinkled specimens result in reflections in Fourier transforms of images that, in the direction perpendicular to the tilt axis, become increasingly blurred at high tilt angles. These effects dramatically reduce high-resolution information in the three-dimensional (3-D) reconstructions of crystalline membranes (Baldwin, et al., 1988; Gyobu, et al., 2004; Henderson, et al., 1990; Hite, et al., 2010; Nogales, et al., 1995; Walz, et al., 1997).

A lot of effort has been made to improve the flatness of crystalline membranes on continuous carbon films by tuning properties such as surface roughness and conductivity (Butt, et al., 1991; Glaeser, 1992; Han, et al., 1994). Specimen-preparation methods such as the sandwich method and the back-injection method were also developed to improve flatness (Booy & Pawley, 1993; Calarco, et al., 1990; Fujiyoshi, 1998; Glaeser, 1992; Gyobu, et al., 2004; Nogales, et al.,

1995; Vonck, 2000; Yoshioka, et al., 2010). However, cryo-EM data collection is usually carried out at liquid nitrogen temperatures, and vitrified specimens are prepared by plunging the blotted grids into liquid ethane. The large change in temperature introduces another artefact, the so-called "cryo-crinkling" problem (Booy & Pawley, 1993). The copper grid shrinks substantially and crinkling of the support film then arises due to the difference in thermal expansion coefficients of carbon and copper. The dimensional changes in a material is given by

$$\Delta L/L = \alpha (T - T_i), \qquad \text{Eq. (1)}$$

where ΔL/L represents the relative change in dimension when the material is cooled from room temperature to liquid nitrogen temperature; T_i is room temperature and T is the temperature of liquid nitrogen; and α is the linear thermal expansion coefficient of the material. Booy and Pawley (Booy & Pawley, 1993) demonstrated that cryo-crinkling can be minimized by replacing the copper grid by a molybdenum grid, since the difference in thermal expansion coefficients of carbon and molybdenum is small. Vonck (Vonck, 2000) illustrated that the flatness of specimens was enhanced by the use of high-quality molybdenum grids with smooth surfaces and wide grid bars. It is now standard to use molybdenum grids for cryo-EM of crystalline membranes.

In this paper, a molybdenum grid with a holey gold film was prepared in order to minimize beam-induced motion and cryo-crinkling simultaneously during automated cryo-EM data collection of crystalline membranes. A continuous carbon film is transferred onto the top of the holy gold film to complete the fabrication of the specimen support. We call these Au/Mo grids, although all of our supports for crystalline membranes also contain a continuous carbon film. We believe that the unique properties of this grid arise from the thermal expansion coefficients of the three components. The thermal expansion coefficient of carbon ($6 \times 10^{-6}\ ^{o}C^{-1}$) is close to that of molybdenum ($5 \times 10^{-6}\ ^{o}C^{-1}$), while gold has a much larger thermal expansion

coefficient (14 x 10^{-6} $^{o}C^{-1}$) and the thermal expansion coefficient of copper is 17 x 10^{-6} $^{o}C^{-1}$. (Haynes, 2015). Contraction of the holey gold film is thus expected to tighten it, along with the crystalline membranes, under tension, rather than cause them to crinkle when the substrate with the specimen is cooled to low temperatures.

The samples that we used to test our grids were crystalline polypeptoid membranes. Polypeptoids are bio-inspired synthetic polymers comprising repeating N-substituted glycine monomer units. They are similar to polypeptides except for the fact that the side chain is appended to the nitrogen atom rather than the α-carbon (Nam, et al., 2010; Robertson, et al., 2014). Crystalline polypeptoid membranes, which are only one unit-cell thick, similar to 2-D protein membranes but with smaller unit cells, are generated by the self-assembly of di-block copolymers in dilute solutions (Jiang, et al., 2018; Jiang, et al., 2019; Xuan, et al., 2019). In a previous study, we have used images of untilted specimens to determine the structure of crystalline polypeptoid membranes with about 2 Å resolution when using vitrified specimens prepared on a holey carbon support film (Jiang, et al., 2018). Contraction of crystalline polypeptoid membrane cannot be accurately predicted since the thermal expansion coefficient of polypeptoid is unknown. However, as a synthetic polymer, the thermal expansion coefficient of polypeptoid is likely to be similar to the thermal expansion coefficients of typical semicrystalline polymers which are at least one order of magnitude larger than carbon film. In this case, the less contracted carbon film on which the crystalline polypeptoid membranes reside makes the change of lattice of membranes less than that of the free-standing membranes.

The performance of the new Au/Mo grid was characterized by quantifying beam-induced motion, flatness of specimens, and resolution. A different grid, which had a continuous thin carbon film on a holey gold film supported on a gold grid, was prepared for comparison. This

grid, which we called an Au/Au grid, is used to confirm the expectation that flatness of specimen is improved when Mo grids are used rather than Au grids, as predicted by the difference in thermal expansion coefficients.

The results indicated that both the Au/Mo and Au/Au grids effectively reduced beam-induced motion in untilted specimens as compare to that of the holey carbon films on copper grids (Russo & Passmore, 2014; Russo & Passmore, 2016). Surprisingly, in view of the similarity observed with untilted grids, the Au/Mo grid showed dramatically less beam-induced motion than the Au/Au grid when images were recorded at 45° tilt. The flatness of specimens was also investigated by measuring the local variation in defocus across the 45° tilt images. Images obtained from Au/Mo grid showed improved flatness of specimens as compared to those obtained from Au/Au grids. Finally, the resolution of images of specimens tilted at about 45°, when supported on the Au/Mo grids, often remains about 1.5 Å, which is better than all previous studies on crystalline polypeptoid membranes. The results thus show that these Au/Mo grids provide excellent performance for imaging very thin crystals of a synthetic polymer. A comparison of the resolution of images obtained with tilted specimens that were prepared on the Au/Au grids has not been undertaken, however.

2. Material and methods

2.1 Preparation of polypeptoid nanosheets

The detailed protocol for polypeptoid synthesis can be found in (Xuan, et al., 2019). Two sequence-defined di-block co-polypeptoid decamers, with four hydrophilic monomers and six hydrophobic monomers, were used in this study. These di-block polypeptoids were composed of the same hydrophilic block of poly(*N*-2-(2-(2-methoxyethoxy)ethoxy)ethylglycine) (Nte) and a

hydrophobic aromatic block bearing either *para*-bromo- or *meta*-bromo-phenylethyl side chains. The di-block copolypeptoid with *para*-substituted bromine atoms was called Nte_4-N4$Brpe_6$ and the di-block copolypeptoid with *meta*-substituted bromine atoms was called Nte_4-N3$Brpe_6$. The chemical structures and characteristics are shown in Figure S1 and Table S1. To form the crystalline membranes, the polypeptoids were dissolved in tetrahydrofuran (THF) /water (1:1, v/v) at a concentration of 2 mg/mL. The solutions were made in glass vials. The caps of the vials were left loose to enable evaporation of THF at 4°C in a refrigerator. After 72 hours, the solution becomes turbid, indicating that sheets have formed but stay in suspension.

2.2 Preparation of Au/Mo and Au/Au grids

The holey gold films were prepared by following the protocol described by Downing (Downing, 2003), which is similar to the method for preparing C-flat grids but different from that of the QUANTIFOIL grids (Quispe, et al., 2007). A microfabricated silicon-template surface was coated by a water-soluble releasing agent layer, Victawet 35B (Ladd Research Inc.), in a thermal evaporator with a rotation stage (Denton 502B). After deposition, a layer of gold of desired thickness (about 50 nm) was evaporated onto the Victawet layer in the same thermal evaporator, maintained continuously under high vacuum ($<10^{-6}$ Torr). A glass slide was placed next to the silicon template so that the gold film thickness could be measured using atomic force microscopy after the gold film was transferred to another glass slide using a protocol as described below.

Molybdenum grids and gold grids (Pacific Grid Tech Inc.) were placed on a filter paper at the bottom of a glass petri dish filled by Mili-Q deionized water. The template with two deposited layers was slowly immersed in water which dissolves the Victawet layer under the

gold film. The template was kept close to the air-water interface so that the gold film peeled off the template and floated at the interface. The floated gold film remained flat due to surface tension at the water-air interface. The water was drained out slowly to lower the gold film on top of grids. The grids were dried out at room temperature on filter paper overnight and then transferred onto a hot plate for annealing. The annealing process (230 ^{o}C for 2 hours) resulted in good adhesion of the holy gold film on the molybdenum and gold grids. A thin carbon layer, about 50 Å thick, was then transferred from mica to the annealed grids, still on the same filter paper, using a similar protocol as that described above, except that carbon was evaporated onto freshly cleaved mica and subsequently floated off onto water in the standard way. It is important to note that the molybdenum grids from Pacific Grid Tech used in this study have wider grid bars and smoother surface which are important to flatten the supporting films. (Vonck, 2000)

2.3 Cryo-EM data collection

A 3 µl droplet of the desired membranes in aqueous suspension was applied to the grid, excess sample was blotted, and the grid was then plunged into liquid ethane to obtain vitrified specimens, using a Vitrobot (FEI Company). The grid was carefully mounted into a specimen cartridge to avoid potential deformation or damage caused by a tweezer in the cryo-transfer station. The quality of mounted grids was checked with a magnifier before cryo-transfer into microscopes.

The specimens were imaged with a JEOL 3200FSC (JEOL Inc.) operated at 300 kV with a K2 Summit direct detection camera and in-column energy filter (slit width at 20 eV), and also with a FEI Krios (FEI Inc.) operated at 300 kV with a K2 Summit direct detection camera and post-column energy filter (slit width at 20 eV). SerialEM was used to record images with defocus values from -0.5 to -2 µm at 0^{o} and 45^{o} tilt. Cryo-EM images of Nte_4-N3Brpe$_6$, recorded on the

JEOL-3200FSC, were used for the characterization of beam-induced motion and flatness of membranes. An electron-illumination area of 2 μm diameter was used so that the beam symmetrically covered the entire hole during recording, in order to avoid any effect of the illumination geometry on the quality of micrographs (Miyazawa, et al., 1999; Russo & Passmore, 2016). Dose-fractionation movies comprised 22 frames for untilted images, and 40 frames for 45° tilt images, respectively. The accumulated dose for each movie was about 20 e/Å^2. Previous studies have shown that Nte_4-N4Brpe$_6$ membranes exhibit a larger number of reflections relative to Nte_4-N3Brpe$_6$ membranes (Xuan, et al., 2019). We therefore collected high-resolution images from tilted specimens of Nte_4-N4Brpe$_6$ membranes using a FEI Krios, since this microscope was expected to have better resolution than the JEOL-3200FSC. Information about the samples, pixel sizes (referred to the specimen), and microscopes used is listed in Table 1. Examples of high-resolution cryo-EM micrographs and Fourier transforms of untilted, frozen-hydrated crystalline membranes are shown in Figure S2. The detailed crystalline structures of crystalline polypeptoid membranes were reported previously in (Xuan, et al., 2019).

2.4 Image analysis

Movie frames were aligned and summed by MotionCorr2 to compensate for beam-induced motion (Li, et al., 2013; Zheng, et al., 2017). Local contrast-transfer function (CTF) estimations were carried out using goCTF (Su, 2019). Tilt axis was determined based on the stage and image shift calibrations in SerialEM on both microscopes. Micrographs recorded using JEOL-3200FSC were rotated by an absolute rotation angle, which was measured in serialEM after calibration, so that the tilt axis was perpendicularly aligned in each image for local defocus estimation as required by goCTF. Areas comprising 2700 pixels on edge were extracted from

each micrograph after rotation. These extracted areas were then subdivided into 8 x 8 boxes, which had 600x600 pixels in each box and a 50% overlap along *x*-*y* directions in the plane, respectively.

The lattice-unbending process developed for crystalline membranes, and the calculation of IQ (image quality) plots, were carried out using 2DX (Gipson, et al., 2007). 60 micrographs obtained at 45° tilt using Au/Mo grids were used for the analysis of IQ and resolution.

3. Results and discussion

A schematic of the holey gold film on the molybdenum grid is shown in Figure 1A. When this grid is cooled, both components shrink. However, there is strong adhesion between the gold film and the molybdenum grid bar. As the holey gold film between the molybdenum grid bars contracts, we expect wrinkles in the carbon film that may have existed before cooling to flatten as the holes in the gold film become larger and the film perhaps also thins. The expected change in linear dimension is small, however; it should be less than 0.2 percent for a temperature change of 200 °C, which would be difficult to observe experimentally. In addition, the spacing between the holes is not expected to change more than by the amount that the entire 3 mm Mo grid itself contracts upon cooling. A potential increase in the hole size and possible flattening of the holey gold film are good features, as both are also expected to flatten the crystalline polypeptoid membranes, which are placed on the carbon film, which, in turn, is stuck to the holey gold film.

Figure 1B shows an optical micrograph of the Au/Mo grid with the carbon film. The molybdenum grid appears dark and the bright circles contain both the holey gold film and carbon film. Figure 1C shows a TEM micrograph of the holey gold film (covered by carbon film) within one of the bright holes in Figure 1B. In order to facilitate the requirements of low-dose image

collection, the pattern of the holey gold film was designed to have small, carbon-coated holes for focusing adjacent to large holes for recording.

In order to compare the stability of our Au/Mo grid with that of our Au/Au grid, the beam-induced motion of untilted crystalline polypeptoid membranes was measured based on the electron micrographs obtained from both grids under identical imaging conditions.

Figure 2A shows the mean displacement and standard deviation of movie frames as a function of accumulated dose for the Au/Mo grids. The first three frames exhibit the largest motion, up to 3.0 Å, while the motion of the following frames decreases monotonically with increasing dose. This is in agreement with literature wherein large beam-induced motion is reported in the first few frames (Brilot, et al., 2012; Li, et al., 2013; Russo & Passmore, 2014; Russo & Passmore, 2016; Zheng, et al., 2017). Figure 2B shows the mean displacement and standard deviation of movie frames as a function of accumulated dose for the Au/Au grids. These data are qualitatively similar to the data in Figure 2A. This indicates that beam-induced motion in the untilted crystalline polypeptoid membranes is effectively the same when using either Au/Mo grids or Au/Au grids.

3-D reconstruction of the structure of crystalline membranes requires data obtained from tilted specimens, however. Comparing the performance of grids under tilted conditions is thus of great importance. Figure 3A shows the mean displacement and standard deviation of frames as a function of accumulated dose for the Au/Mo grids at 45°. Although increased by about a factor of 2, these data are still qualitatively similar to the data in Figure 2A. In other words, beam-induced motion of specimens supported on Au/Mo grids is similar in both tilted and untilted samples.

Figure 3B, on the other hand, shows the mean displacement and standard deviation of frames as a function of accumulated dose for the Au/Au grids at 45°. Surprisingly, the first few

frames now show ~10-fold larger motion than what is observed with Au/Mo grids. The mean movement between the first and second frame was 55 Å when using Au/Au grids, and even up to an accumulated dose of 5 $e/Å^2$ or more, the mean displacement between successive frames remains greater than 5 Å. This result indicates that beam-induced motion in the highly tilted crystalline polypeptoid membranes can be minimized much more effectively by using Au/Mo grids than is possible for Au/Au grids. The same data plotted on the different scales, which further demonstrates the differences in motion observed with the Au/Mo and Au/Au grids, are shown in Figure S3.

We attribute the greater motion observed with highly tilted Au/Au grids to one or both of two effects. There may be some initial crinkling of the holey gold support film, produced at the time that the grids were made, which is partially removed when Au/Mo grids are cooled, but which remains unaltered when Au/Au grids are cooled. In addition, there is much less risk of the grid itself being bent during handling, and thus the specimen also becoming crinkled, when Mo grids are used. This is because Mo grids are much less compliant than Au grids. Russo and Passmore have, in fact, emphasized that great care must be taken to ensure that Au/Au grids are not bent during handling (Russo & Passmore, 2016).

The results obtained with our Au/Au grids cannot be compared to the results obtained with UltrAuFoil grids [19, 20], however, nor was it our intent to do so here. Rather, our intent was to determine whether, in practice, the use of molybdenum grids rather than gold grids actually produced the beneficial effect that was expected on physical grounds.

Our Au/Au grids and commercially available UltrAuFoil grids are, in fact, made using different methods, and thus they may thus have different structures and degrees of flatness prior to cooling. One significant difference is that the initial, holey-polymer film, which is used as the

starting point for fabrication of UltrAuFoil grids, seems to be pulled down within the open area between metal grid bars, and thus it already appears to be stretched and pulled tight. A second difference is that we intentionally used the same technique to mechanically handle our Au/Au grids as when handling our much stiffer Au/Mo grids. In view of the caution expressed in (Russo & Passmore, 2016), it thus is possible that our Au/Au grids may have become crinkled as a result of handling. Finally, our grids are required to have a thin carbon film laid over the holey gold, and neither the holey gold nor the continuous carbon may remain perfectly flat during the operation of transferring the carbon film.

The difference between local and global defocus values in a micrograph is a measure of flatness variation. The local defocus values of more than 150 micrographs each, for both Au/Au and Au/Mo grids, were determined by the software package goCTF (Su, 2019). Two micrographs, which exhibit the smallest and the largest deviations seen in the data set, are shown in Figure 4. Figure 4A shows a plot of local defocus values as a function of position in the micrograph of an especially flat, tilted sample on the Au/Mo grid. Also shown in Figure 4A is a plane that was fitted to the data using bilinear regression. We refer to the difference of local defocus value from the fitted value as being the deviation at each position in a micrograph. When grids are tilted by 45°, the deviation is ~1.4 times the height above or below the plane of the specimen.

Figure 4B shows an example of the deviation at each position based on the measurements shown in Figure 4A as shown in filled contour map. The deviation values are shown in different colors in a range from -500 to 500 Å. The root mean square deviation (RMSD) is defined as

$RMSD = \sqrt[2]{\sum_{j=1}^{m} (defocus_j^{measured} - defocus_j^{fitting})^2 / m}$, where m is the number of positions in a micrograph. The RMSD for this micrograph was 101 Å, which was the smallest value in the analyzed micrographs. Figure 4C shows a plot of local defocus values as a function of position in the micrograph of a more wrinkled, tilted sample on the Au/Mo grid, and the deviation plot is shown in Figure 4D. The RMSD for this micrograph was 310 Å which was the largest values in the analyzed micrographs.

It is difficult to determine whether the deviations shown in Figures 4 A and 4B are just due to small errors due to the fact that low-dose images are noisy, or whether they reflect real variations in local defocus values due to crinkling of the specimen. What can be said, however, is that deviations from the fitting that are greater than what is shown in Figures 4A and 4B must be due to crinkling, since the noise level was the same across all images. The contour map of deviations shown in Figures 4B and 4D revealed that the deviations appear to be locally correlated for both positive and negative values, which are shown as the connected areas with color gradient. This local correlation suggests the deviations were induced by the presence of crinkling rather than the random noise inherent in defocus estimation.

A histogram of all RMSD values is shown in Figure 5. Comparison of Figures 5A and B indicates that the RMSD in the case of the Au/Mo grid is significantly smaller and has a narrower distribution. The mean values of RMSD (148 Å) obtained from the Au/Mo grid is significantly lower than that (260 Å) from the Au/Au grid. It is noteworthy that there was no apparent bowing or buckling within the field of view of micrographs collected from single holes. Instead, the local defocus measurement in a micrograph is well-accounted by a plane with only small, local deviations from the global plane, rather than by a parabolically curved surface.

Finally, we find that the improved flatness of the support film, which is obtained after cooling Au/Mo grids to liquid nitrogen temperature, correlates with obtaining images of excellent quality. This point is documented by the IQ plots, obtained after applying lattice unbending, for untilted crystalline polypeptoid membrane (Nte_4-N4Brpe$_6$) on Au/Mo grids, such as the example shown in Figure 6A. Image quality (IQ) is a measure of signal-to-noise ratio (SNR) which indicates the expected phase error at each reflection in Fourier space. Such plots give a visualization of the strength of reflections and, thus, the maximum resolution at which high-resolution information is reliable (Glaeser, 2007; Henderson, et al., 1986). Smaller IQ values represent higher SNR and small phase error, and they are thus represented by larger squares. Reflections with IQ values smaller than 7 are generally acceptable for analysis, since the expected phase error is less than 45 degrees. Thus, we use the IQ value of 6 (phase error less than 39 degrees) as the threshold for the IQ plots and for our analysis of data obtained from tilted specimens. Resolution rings are drawn at 24, 12, 4, 2 and 1.5 Å in Figure 6A. It is evident that IQ = 2 spots, for which the expected phase error is less than 9 degrees, can be observed to a resolution of about 1.8 Å.

Figure 6B shows the IQ plot of a crystalline polypeptoid membrane (Nte_4-N4Brpe$_6$) on Au/Mo grid at 45^o tilt, again after lattice unbending. The lines labeled TAXA in Figure 6 represent the axis of tilt. The IQ plot in Figure 6B is geometrically deformed in order that the reciprocal lattice is shown in a way that is comparable to that of an untilted projection. Note that this distortion converts the circles, at given values of resolution, into ellipses. This intentional distortion has been applied in order to facilitate comparison with Figure 6A. Figure 6B shows IQ=3 spots, for which the expected phase error is still only 14 degrees, up to a resolution of

about 1.5 Å. Furthermore, high-resolution data are preserved not only along the direction parallel to the tilt axis but also along the direction perpendicular to the tilt axis.

A summary of IQ values and resolution obtained from the 45° tilted specimens are shown in Table 2. This summary is based on what we deemed to be the 60 best micrographs, out of a total of 125 obtained during automated data collection (micrographs without crystals and micrographs with overlapped crystals were excluded). These 60 micrographs were subsequently processed using the lattice-unbending software 2DX. It is evident that significant structural information with reliable phase error (less than 39 degrees), up to 1.5 Å, was obtained from the tilted crystalline polypeptoid membranes at 45° tilt using Au/Mo grids.

It is well-known that the reflections normally become blurred along the direction perpendicular to the tilt axis if the specimen is not flat. The results in Figure 6 and Table 2 thus indicate that the Au/Mo grid can be used to obtain, for the first time, high-resolution images of the crystalline polypeptoid membranes in both tilted and non-tilted geometries. A comparison of the resolution of the 3-D reconstructed maps obtained with the commercial UltrAufoil grids will be carried out in future work.

4. Conclusions

In summary, we have fabricated a novel Au/Mo grid for high-resolution cryo-EM data collection. It comprised a holey gold film transferred onto a molybdenum EM grid. A continuous thin carbon film was then transferred onto the holey gold film to support the crystalline polypeptoid membranes. The amount of beam-induced motion was measured to quantify the stability of Au/Mo grids in both tilted and non-tilted configurations under cryogenic conditions. In addition, measurements of local defocus values of tilted membranes were used to quantify the

flatness of specimens. Micrographs of tilted specimens, after using the lattice-unbending software 2DX, show high-resolution information of the membranes, up to 1.5 Å, both parallel and perpendicular to the tilt axis. We conclude that the new Au/Mo grid provides excellent performance for imaging very thin crystals of a synthetic polymer by simultaneously minimizing cryo-crinkling and beam-induced motion.

Supplementary materials

Figure S1 to S3 and Table S1

Conflicts of interest

The authors declare no competing financial interest.

Note

This study was originally conceived by Dr. Kenneth H. Downing who passed away before the work was finished. He played an active role until the decease.

Acknowledgements

Funding for this work was provided by the Soft Matter Electron Microscopy Program (KC11BN), supported by the Office of Science, Office of Basic Energy Science, US Department of Energy, under Contract DE-AC02-05CH11231. Work at the Molecular Foundry was supported by the Office of Science, Office of Basic Energy Sciences, of the U.S. Department of Energy under Contract No. DE-AC02-05CH11231. We gratefully acknowledge the help provided from many discussions with Dr. Bong-Gyoon Han at the Lawrence Berkeley National Laboratory. Micrographs presented here were collected at the Donner Cryo-EM resources in

Lawrence Berkeley National Lab and at the Berkeley Bay Area Cryo-EM facility in University of California Berkeley.

References:

BALDWIN, J.M., HENDERSON, R., BECKMAN, E. & ZEMLIN, F. (1988). Images of Purple Membrane at 2.8 a Resolution Obtained by Cryo-Electron Microscopy. J Mol Biol **202**(3), 585-591.

BOOY, F.P. & PAWLEY, J.B. (1993). Cryo-Crinkling - What Happens to Carbon-Films on Copper Grids at Low-Temperature. Ultramicroscopy **48**(3), 273-280.

BRILOT, A.F., CHEN, J.Z., CHENG, A.C., PAN, J.H., HARRISON, S.C., POTTER, C.S., CARRAGHER, B., HENDERSON, R. & GRIGORIEFF, N. (2012). Beam-induced motion of vitrified specimen on holey carbon film. Journal of structural biology **177**(3), 630-637.

BUTT, H.J., WANG, D.N., HANSMA, P.K. & KUHLBRANDT, W. (1991). Effect of Surface-Roughness of Carbon Support Films on High-Resolution Electron-Diffraction of 2-Dimensional Protein Crystals. Ultramicroscopy **36**(4), 307-318.

CALARCO, P.G., PEACHEY, L.D., WILLIAMS, D.B., AMERICA, E.M.S.O., MICROSCOPY, I.C.O.E., MICROSCOPY, I.F.O.S.F.E. & SOCIETY, M.A. (1990). *Electron Microscopy 1990: Proceedings of the XIIth International Congress for Electron Microscopy Held in Seattle, Washington, USA - 48th Annual Meeting of the Electron Microscopy Society of America and 25th Annual Meeting of the Microbeam Analysis Society. Biological sciences*. San Francisco Press.

CHENG, Y.F. (2015). Single-Particle Cryo-EM at Crystallographic Resolution. Cell **161**(3), 450-457.

DOWNING, K.H. (2003). Support Films with Uniform Hole Size. Microscopy Today **11**(5), 54-54.

FUJIYOSHI, Y. (1998). The structural study of membrane proteins by electron crystallography. Adv Biophys **35**, 25-80.

GIPSON, B., ZENG, X., ZHANG, Z.Y. & STAHLBERG, H. (2007). 2dx--user-friendly image processing for 2D crystals. Journal of structural biology **157**(1), 64-72.

GLAESER, R.M. (1992). Specimen Flatness of Thin Crystalline Arrays - Influence of the Substrate. Ultramicroscopy **46**(1-4), 33-43.

GLAESER, R.M. (2007). *Electron crystallography of biological macromolecules*. Oxford ; New York: Oxford University Press.

GLAESER, R.M., MCMULLAN, G., FARUQI, A.R. & HENDERSON, R. (2011). Images of paraffin monolayer crystals with perfect contrast: Minimization of beam-induced specimen motion. Ultramicroscopy **111**(2), 90-100.

GYOBU, N., TANI, K., HIROAKI, Y., KAMEGAWA, A., MITSUOKA, K. & FUJIYOSHI, Y. (2004). Improved specimen preparation for cryo-electron microscopy using a symmetric carbon sandwich technique. Journal of structural biology **146**(3), 325-333.

HAN, B.G., WOLF, S.G., VONCK, J. & GLAESER, R.M. (1994). Specimen Flatness of Glucose-Embedded Biological-Materials for Electron Crystallography Is Affected Significantly by the Choice of Carbon Evaporation Stock. Ultramicroscopy **55**(1), 1-5.

HAYNES, W.M. (2015). *Handbook of Chemistry and Physics*. CRC Press.

HENDERSON, R., BALDWIN, J.M., CESKA, T.A., ZEMLIN, F., BECKMANN, E. & DOWNING, K.H. (1990). Model for the Structure of Bacteriorhodopsin Based on High-Resolution Electron Cryomicroscopy. J Mol Biol **213**(4), 899-929.

HENDERSON, R., BALDWIN, J.M., DOWNING, K.H., LEPAULT, J. & ZEMLIN, F. (1986). Structure of Purple Membrane from Halobacterium-Halobium - Recording, Measurement and Evaluation of Electron-Micrographs at 3.5 a Resolution. Ultramicroscopy **19**(2), 147-178.

HENDERSON, R. & GLAESER, R.M. (1985). Quantitative-Analysis of Image-Contrast in Electron-Micrographs of Beam-Sensitive Crystals. Ultramicroscopy **16**(2), 139-150.

HITE, R.K., SCHENK, A.D., LI, Z.L., CHENG, Y.F. & WALZ, T. (2010). Collecting Electron Crystallographic Data of Two-Dimensional Protein Crystals. Methods in Enzymology, Vol 481: Cryo-Em, Part a - Sample Preparation and Data Collection **481**, 251-282.

JIANG, X., GREER, D.R., KUNDU, J., OPHUS, C., MINOR, A.M., PRENDERGAST, D., ZUCKERMANN, R.N., BALSARA, N.P. & DOWNING, K.H. (2018). Imaging Unstained Synthetic Polymer Crystals and Defects on Atomic Length Scales Using Cryogenic Electron Microscopy. Macromolecules **51**(19), 7794-7799.

JIANG, X., XUAN, S.T., KUNDU, J., PRENDERGAST, D., ZUCKERMANN, R.N. & BALSARA, N.P. (2019). Effect of processing and end groups on the crystal structure of polypeptoids studied by cryogenic electron microscopy at atomic length scales. Soft Matter **15**(23), 4723-4736.

KUHLBRANDT, W. (2014). The Resolution Revolution. Science **343**(6178), 1443-1444.

KUHLBRANDT, W., WANG, D.N. & FUJIYOSHI, Y. (1994). Atomic Model of Plant Light-Harvesting Complex by Electron Crystallography. Nature **367**(6464), 614-621.

LI, X.M., MOONEY, P., ZHENG, S., BOOTH, C.R., BRAUNFELD, M.B., GUBBENS, S., AGARD, D.A. & CHENG, Y.F. (2013). Electron counting and beam-induced motion correction enable near-atomic-resolution single-particle cryo-EM. Nat Methods **10**(6), 584-+.

MIYAZAWA, A., FUJIYOSHI, Y., STOWELL, M. & UNWIN, N. (1999). Nicotinic acetylcholine receptor at 4.6 angstrom resolution: Transverse tunnels in the channel wall. J Mol Biol **288**(4), 765-786.

NAM, K.T., SHELBY, S.A., CHOI, P.H., MARCIEL, A.B., CHEN, R., TAN, L., CHU, T.K., MESCH, R.A., LEE, B.C., CONNOLLY, M.D., KISIELOWSKI, C. & ZUCKERMANN, R.N. (2010). Free-floating ultrathin two-dimensional crystals from sequence-specific peptoid polymers. Nat Mater **9**(5), 454-460.

NOGALES, E., WOLF, S.G., KHAN, I.A., LUDUENA, R.F. & DOWNING, K.H. (1995). Structure of Tubulin at 6.5 Angstrom and Location of the Taxol-Binding Site. Nature **375**(6530), 424-427.

QUISPE, J., DAMIANO, J., MICK, S.E., NACKASHI, D.P., FELLMANN, D., AJERO, T.G., CARRAGHER, B. & POTTER, C.S. (2007). An improved holey carbon film for cryo-electron microscopy. Microsc Microanal **13**(5), 365-371.

RHINOW, D. & KUHLBRANDT, W. (2008). Electron cryo-microscopy of biological specimens on conductive titanium-silicon metal glass films. Ultramicroscopy **108**(7), 698-705.

ROBERTSON, E.J., OLIVER, G.K., QIAN, M., PROULX, C., ZUCKERMANN, R.N. & RICHMOND, G.L. (2014). Assembly and molecular order of two-dimensional peptoid nanosheets through the oil-water interface. P Natl Acad Sci USA **111**(37), 13284-13289.

RUSSO, C.J. & PASSMORE, L.A. (2014). Ultrastable gold substrates for electron cryomicroscopy. Science **346**(6215), 1377-1380.

RUSSO, C.J. & PASSMORE, L.A. (2016). Ultrastable gold substrates: Properties of a support for high-resolution electron cryomicroscopy of biological specimens. Journal of structural biology **193**(1), 33-44.

SCHERES, S.H. (2012). RELION: implementation of a Bayesian approach to cryo-EM structure determination. Journal of structural biology **180**(3), 519-530.

SPENCE, J.C.H., WEIERSTALL, U., FRICKE, T.T., GLAESER, R.M. & DOWNING, K.H. (2003). Three-dimensional diffractive imaging for crystalline monolayers with one-dimensional compact support. Journal of structural biology **144**(1-2), 209-218.

SU, M. (2019). goCTF: Geometrically optimized CTF determination for single-particle cryo-EM. Journal of structural biology **205**(1), 22-29.

TAN, Y.Z., BALDWIN, P.R., DAVIS, J.H., WILLIAMSON, J.R., POTTER, C.S., CARRAGHER, B. & LYUMKIS, D. (2017). Addressing preferred specimen orientation in single-particle cryo-EM through tilting. Nat Methods **14**(8), 793-+.

VONCK, J. (1996). A three-dimensional difference map of the N intermediate in the bacteriorhodopsin photocycle: Part of the F helix tilts in the M to N transition. Biochemistry **35**(18), 5870-5878.

VONCK, J. (2000). Parameters affecting specimen flatness of two-dimensional crystals for electron crystallography. Ultramicroscopy **85**(3), 123-129.

WALZ, T., HIRAI, T., MURATA, K., HEYMANN, J.B., MITSUOKA, K., FUJIYOSHI, Y., SMITH, B.L., AGRE, P. & ENGEL, A. (1997). The three-dimensional structure of aquaporin-1. Nature **387**(6633), 624-627.

XUAN, S.T., JIANG, X., SPENCER, R.K., LI, N.K., PRENDERGAST, D., BALSARA, N.P. & ZUCKERMANN, R.N. (2019). Atomic-level engineering and imaging of polypeptoid crystal lattices. P Natl Acad Sci USA **116**(45), 22491-22499.

YOSHIOKA, C., CARRAGHER, B. & POTTER, C.S. (2010). Cryomesh (TM): A New Substrate for Cryo-Electron Microscopy. Microsc Microanal **16**(1), 43-53.

ZHENG, S.Q., PALOVCAK, E., ARMACHE, J.P., VERBA, K.A., CHENG, Y.F. & AGARD, D.A. (2017). MotionCor2: anisotropic correction of beam-induced motion for improved cryo-electron microscopy. Nat Methods **14**(4), 331-332.

Table 1. Summary of cryo-EM data collection

Grids	Carbon thickness	Polypeptoid membranes	Total dose	Tilt angle (frame)	Pixel size on sample
Au/Mo [a]	50 Å	Nte_4-N3Brpe_6	20 e/Å	0° (22)	0.51 Å
				45° (40)	1.03 Å
Au/Au [a]	50 Å	Nte_4-N3Brpe_6	20 e/Å	0° (22)	0.51 Å
				45° (40)	1.03 Å
Au/Mo [b]	50 Å	Nte_4-N4Brpe_6	20 e/Å	0° (20)	0.56 Å
				45° (20)	0.56 Å

a. Data was collected using JEOL-3200FSC at 300KeV with K2 and energy filter.

b. Data was collected using FEI Krios at 300KeV with K2 and energy filter.

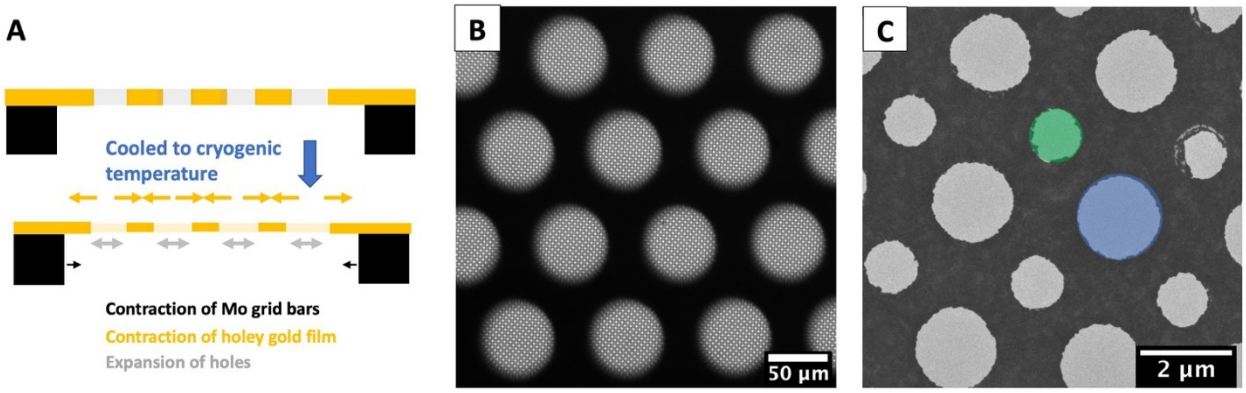

Figure 1. A. Schematic cartoon showing the hypothesized expansion of holes in the holey gold film due to contraction of the gold film relative to the molybdenum grid after cooling. Wrinkles in the carbon film covering the holes, which may have existed before cooling, can be flattened by increasing the size of the holes, and even the holey gold film itself may become flattened as it contracts relative to the Mo grid. Black and yellow represent molybdenum and gold, respectively. Only a few holes are shown and hole expansion is exaggerated for clarity. **B.** Optical microscopy image shows the morphology of holey gold film on a molybdenum grid with a thin carbon film. **C.** TEM micrograph shows the configuration of holes where the blue large hole is used for recording and green small hole is used for focusing in low-dose imaging mode. This image is obtained by magnifying one of the holes in B.

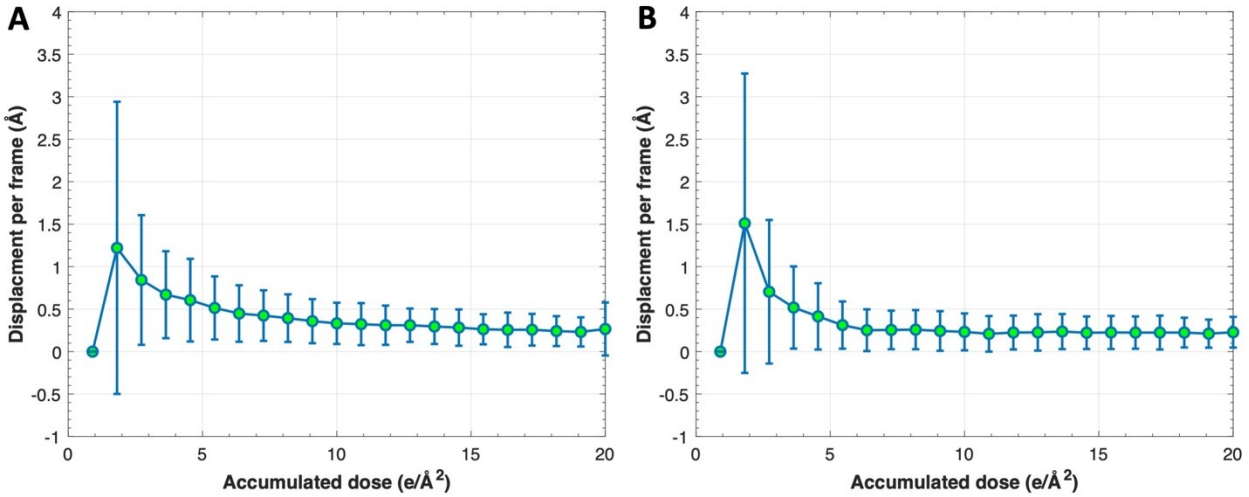

Figure 2. Mean beam-induced displacement and standard deviation of untilted of Nte_4-N3$Brpe_6$ crystalline polypeptoid membranes under cryogenic conditions on the **A.** Au/Mo grid, and **B.** Au/Au grid**.** 109 and 287 micrographs were analyzed from the Au/Mo and Au/Au grids, respectively.

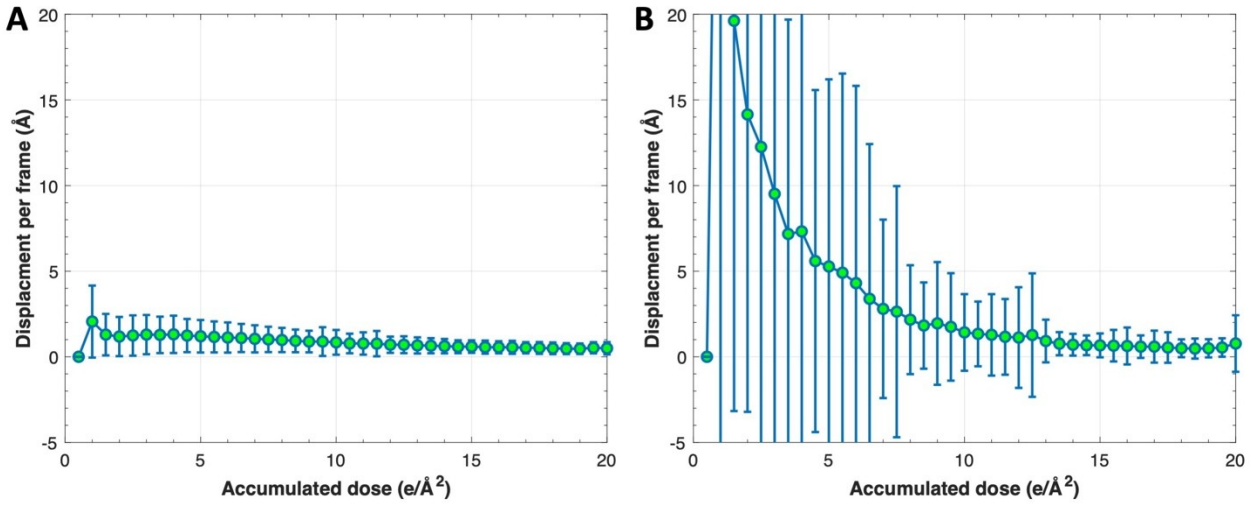

Figure 3. Mean beam-induced displacement and standard deviation of tilted of Nte_4-N3$Brpe_6$ crystalline polypeptoid membranes under cryogenic conditions on the **A.** Au/Mo grid, and **B.** Au/Au grid**.** The same data, when plotted on the different scales, are shown in Figure S3. 291 and 297 micrographs were analyzed of specimens with a tilt angle of 45° supported on the Au/Mo and Au/Au grids, respectively.

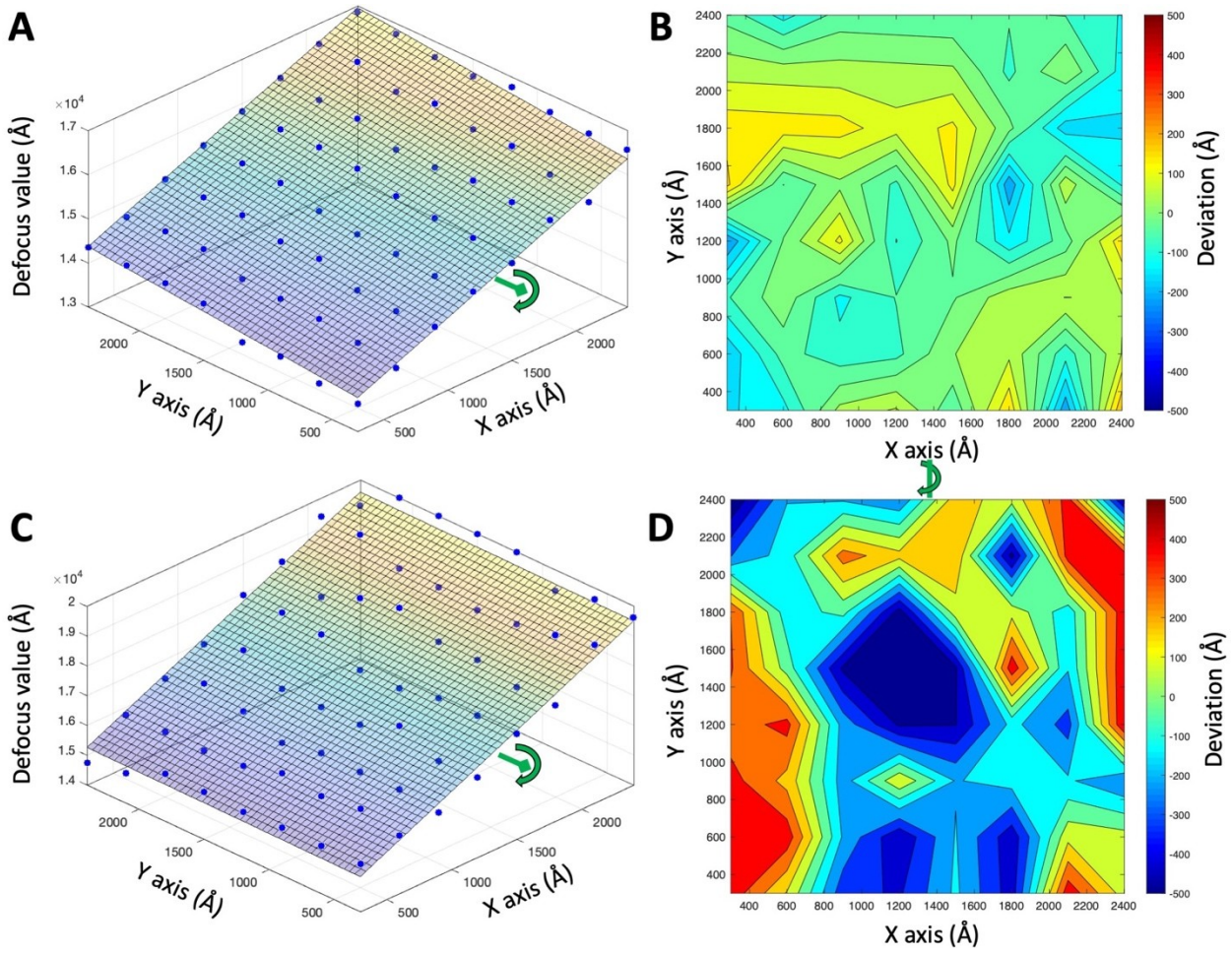

Figure 4. Local defocus estimation of two micrographs that were obtained from a specimen supported (Nte_4-N3$Brpe_6$ crystalline membranes) on the Au/Mo grid, tilted by 45°. 8 x 8 boxes were placed across the micrograph. **A.** A tilted plane has been fitted to the local defocus values, shown as blue dots. The colored plane shows the defocus gradient perpendicular to the tilt axis. The green arrows indicate the tilt axis in the micrograph. **B.** The filled contour map represents the deviation between the measured local defocus value and the fitted defocus value in **A**. **C** and **D** show a micrograph that exhibits the largest deviation, while data for the micrograph with the smallest deviation are shown in **A** and **B.**

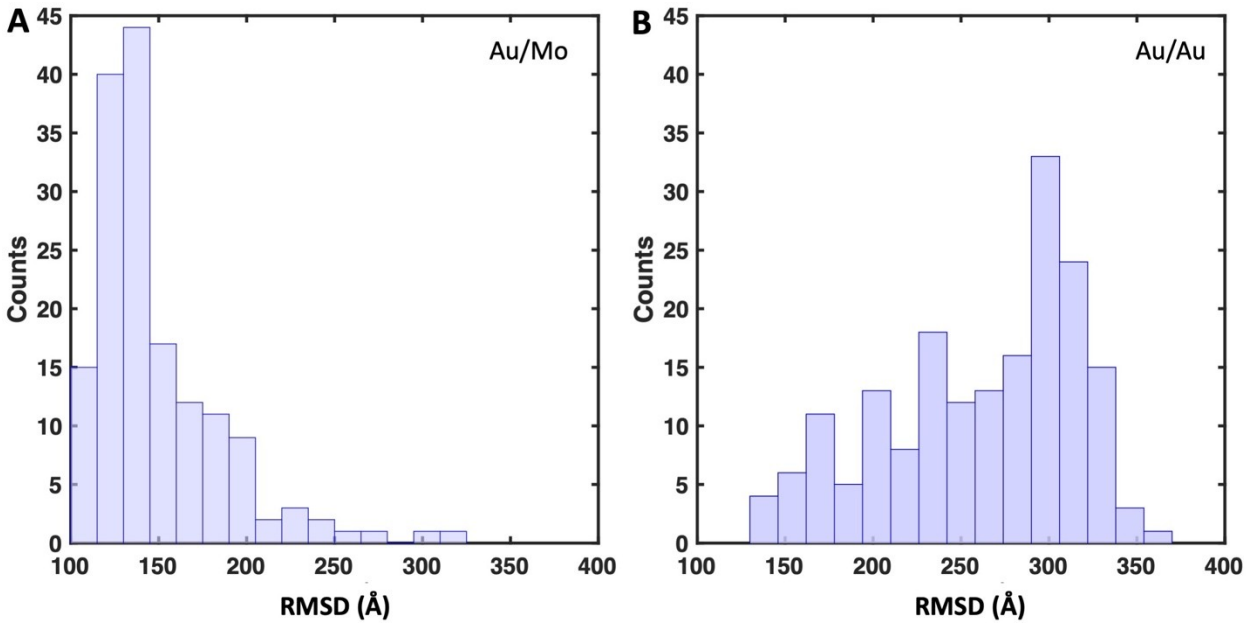

Figure 5. Histograms of RMSD defocus values for 159 micrographs obtained from a Au/Mo grid and 182 micrographs obtained from a Au/Au grid with Nte_4-N3$Brpe_6$ crystalline membranes, tilted by 45°. Root mean squared deviation (RMSD) is used to represent the flatness of crystalline membranes in the collected micrographs by comparing the measured local defocus value to the fitted defocus value at each location in a micrograph. **A.** Histograms of RMSD obtained from micrographs on the Au/Mo grids; **B.** Histograms of RMSD obtained from micrographs on the Au/Au grids.

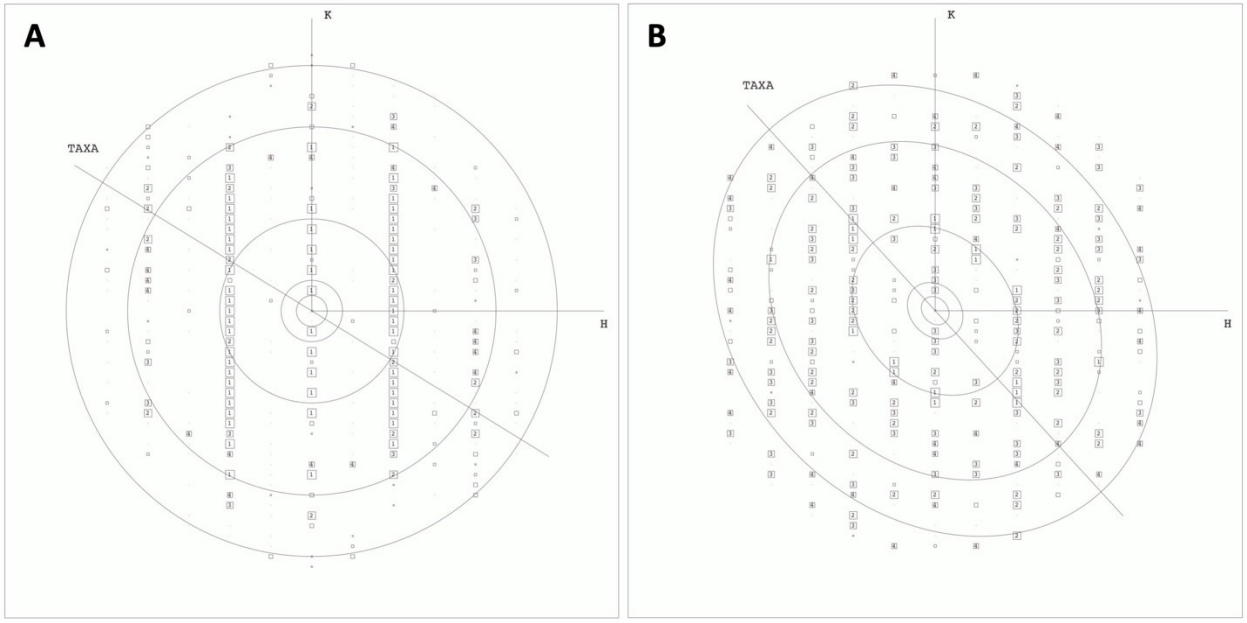

Figure 6. A. The IQ plot of an untilted Nte_4-N4Brpe_6 crystalline membrane specimen on Au/Mo grid, after lattice unbending. **B.** The IQ plot of a specimen on Au/Mo grid, tilted by 45°, after lattice unbending. This IQ plot is intentionally distorted here, as if it were for an untilted projection, i.e., the reciprocal lattice points are shifted to coincide with those for an untilted specimen. TAXA represents the crystal tilt axis, using the terminology in 2DX. Resolution rings are drawn in both cases at 24, 12, 4, 2 and 1.5 Å. Image quality index (IQ) 1–6 of reflections in resolution ranges from zero to Nyquist (1.1 Å) are shown as squares with correspondingly smaller size, reflecting their diminishing statistical reliability.

Table 2. The number of reflections within various zones of resolution, with a given IQ value, in a data set obtained from tilted specimens on Au/Mo grids [a]

Res\IQ	1	2	3	4	5	6
24.0-12.0 Å	21	14	17	8	4	5
12.0-4.0 Å	230	380	154	66	60	59
4.0-2.0 Å	199	699	320	151	130	113
2.0-1.5 Å	23	263	432	423	347	332
1.5-1.1 Å	0	6	34	26	36	29

[a] 60 micrographs obtained at 45° tilt using three Au/Mo grids were used for analysis. Data analysis was carried out on crystalline polypeptoid membranes after lattice-unbending in 2DX.